

Machine learning-assisted antenna modelling for realistic assessment of incident power density on non-planar surfaces above 6 GHz

Ante Kapetanović and Dragan Poljak

Faculty of Electrical Engineering, Mechanical Engineering and Naval Architecture (FESB), University of Split, R. Boškovića 32, 21000 Split, Croatia

*Corresponding author: akapet00@gmail.com

Abstract

In this paper, the analysis of exposure reference levels is performed for the case of a half-wavelength dipole antenna positioned in the immediate vicinity of non-planar body parts. The incident power density (IPD) spatially averaged over the spherical and cylindrical surface is computed at the 6–90 GHz range, and subsequently placed in the context of the current international guidelines and standards for limiting exposure to electromagnetic (EM) fields which are defined considering planar computational tissue models. As numerical errors are ubiquitous at such high frequencies, the spatial resolution of EM models needs to be increased which in turn results in increased computational complexity and memory requirements. To alleviate this issue, we hybridise machine learning and traditional scientific computing approaches through differentiable programming paradigm. Findings demonstrate a strong positive effect the curvature of non-planar models has on the spatially averaged IPD with up to 15% larger values compared to the corresponding planar model in considered exposure scenarios.

Introduction

The over-saturation of the available frequency spectrum, ever increased need for higher data rates, transmission security and connection reliability have all led to the development of the fifth-generation (5G) wireless communication technology, currently in the deployment phase world-wide⁽¹⁾. Two frequency ranges have been utilised for 5G: Frequency Range 1 (FR1), which includes sub-6 GHz bands with extensions up to 7.125 GHz⁽²⁾, and Frequency Range 2 (FR2), which includes bands from 24.25 to 52.6 GHz⁽³⁾. Given the fact that operating frequencies of 5G hand-held devices may fall into the millimetre wave (mmW) spectrum within FR2⁽⁴⁾, hitherto poorly researched from the perspective of human exposure to radio-frequency (RF) non-ionising radiation⁽⁵⁾, it is necessary to reevaluate the interaction with the human body and define appropriate dose metrics.

RF electromagnetic (EM) fields may affect the human body via three primary biological coupling mechanisms, i.e., the nerve stimulation and changes in the cell membrane permeability at lower, and the temperature rise at higher frequencies, especially at mmW⁽⁶⁾. The scientifically proven, potentially hazardous effect

RF radiation at mmW may cause is manifested through the excessive heating of the exposed tissue surface⁽⁷⁾. To prevent tissue damage and to ensure safety by limiting exposure, various international bodies have defined frequency-dependent dosimetric quantities that correlate with the increase in tissue temperature. The International Commission on Non-Ionizing Radiation Protection (ICNIRP) guidelines⁽⁸⁾ and Institute of Electrical and Electronics Engineers (IEEE)/International Committee on Electromagnetic Safety (ICES) standard⁽⁹⁾ have been updated recently with the absorbed or epithelial power density (APD) defined as the basic restriction (BR) or dosimetric reference limit (DRL), respectively, above the transition frequency set to 6 GHz. Volume-averaged specific absorption rate (SAR) should be used as BR/DRL below 6 GHz as it is better correlated with induced temperature rise from RF heating^(10–12). According to the ICNIRP guidelines, APD spatially averaged on a square 4 cm² area accurately approximates the local maximum temperature rise when the field distribution is close to uniform over the surface⁽¹³⁾. To account for the extremely focused beams above 30 GHz, the averaging should additionally be performed over a

square 1 cm² area, where the value of APD must be less than twice the value obtained on 4 cm² area⁽¹⁴⁾. The evaluation plane area of 4 cm² (or 1 cm²) corresponds closely to the front surface of 10 g (or 1 g) cube of tissue with the assumed mass density of 1000 kg m⁻³ used for SAR evaluation at lower frequencies⁽¹⁵⁾. In order to ensure more practical estimation of human exposure, the reference level (RL) and exposure reference level (ERL) have been derived from the BR and DRL, respectively, and are defined by means of the incident power density (IPD). Above 6 GHz, IPD should be spatially averaged over a two-dimensional (2-D) evaluation plane to quantify local exposure. It has proven to be a valid proxy for local temperature rise via human^(16, 17) and animal studies⁽¹⁸⁾, further verified by recent computational efforts^(19–26).

Planar body models have been utilised in the assessment of the spatially averaged IPD where geometrical properties of realistic tissues by means of curvature, edges or other irregularities have not been taken into consideration. For non-planar body parts with the curvature radius on the same scale as the wavelength of the incident field, planar approximation can lead to the incorrect estimation of IPD⁽²⁷⁾. The accurate averaging procedure of IPD over a spherical surface is presented in⁽²⁸⁾, where it has been shown that IPD spatially averaged on a spherical surface may reach up to 30% larger values compared with planar averaging surfaces in equivalent exposure scenarios. Although the quantities retrieved using non-planar models are inherently more accurate, the finite spatial resolution at mmW may induce numerical errors. Thus, the resolution of EM models needs to be significantly higher in comparison with lower frequencies which in turn drastically increases computational time complexity and memory requirements.

To alleviate this issue, computational models in this study are aided with machine learning (ML) and its associated tooling. This peculiar hybridisation is often referred to as differential programming⁽²⁹⁾—a paradigm in scientific computing that allows computational models of physical problems to rebuild (parts of) themselves by a gradient-based optimisation via automatic differentiation⁽³⁰⁾. The effectiveness of automatic differentiation by means of increased speed and accuracy in the assessment of APD at mmW is previously demonstrated in⁽³¹⁾. In addition to the spherical one⁽²⁸⁾, a cylindrical model is introduced in this study as most of the body parts in common exposure scenarios (e.g., an ear during a phone call, a finger while browsing) correspond better to the geometrical characteristics of the cylinder.

The remainder of this paper is outlined as follows. In Materials and methods, the exposure set-up consisting of a single dipole antenna in the immediate vicinity of

a non-planar body part is described. The mathematical formulation of IPD is derived upon the definition of the Poynting vector in free space. In Results and discussion, results of the analysis are demonstrated. Finally, concluding remarks and the contribution of the paper are given in the last section.

Materials and methods

EM exposure scenarios

A simple exposure set-up in which a 5G hand-held device whose antenna is placed in close proximity of a human tissue is analysed. The antenna model is defined as a half-wavelength dipole operating at 6–90 GHz. The analysis is performed assuming free space conditions to evaluate IPD averaged on the surface of the irradiated model at different separation distances ranging from 2 to 150 mm. The computational model of an antenna and the EM simulation are described in detail in the following two subsections.

Three different shapes have been considered to model an exposed body part: a block (de facto standard in dosimetry research⁽³²⁾), a sphere⁽²⁸⁾ and a cylinder. IPD should be spatially averaged over either 4 or 1 cm² area, depending on the frequency. Thus, spatial distribution of points in which the EM field is computed is slightly different for the planar, spherical and cylindrical model. Aforementioned evaluation points along with unit vector field normal to the planar averaging surface at $f < 30$ GHz is shown in Figure 1(a), and is used as a reference in the subsequent analysis.

The spherical and cylindrical averaging surface at $f < 30$ GHz are shown in Figure 1(b) and Figure 1(c), respectively. For both non-planar averaging surfaces, the curvature is dictated by the preset radius ranging from 5 to 15 cm. The overall curvature has a strong effect on the shape of the averaging surface. Nevertheless, all averaging surfaces have the same area at corresponding frequencies.

Computational antenna model

A centre-fed half-wavelength dipole of length L and radius a , driven by a voltage source fixed at 1 V, is used as the antenna model. Its placement in free space is visually represented in Figure 2.

The current distribution along the dipole is obtained by solving the Pocklington integro-differential equation⁽³³⁾

$$E_x^{exc} = j\omega \frac{\mu_0}{4\pi} \int_L I(x') g_a(x, x') dx' - \frac{1}{j4\pi\omega\epsilon_0} \frac{\partial}{\partial x} \int_L \frac{\partial I(x')}{\partial x'} g_a(x, x') dx', \quad (1)$$

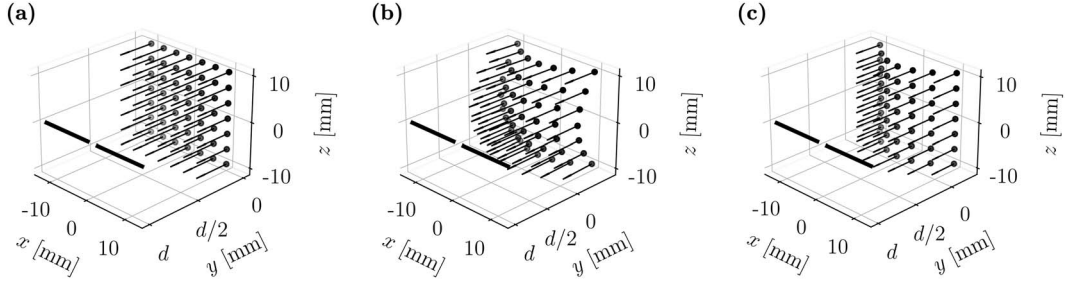


Figure 1. Spatial distribution of points in which the EM field is computed to determine the spatially averaged IPD below 30 GHz on the (a) planar, (b) spherical and (c) cylindrical model. The black arrows depict the unit vector field normal to a surface. The thick dashed line represents the dipole antenna of normalised length with respect to the operating frequency.

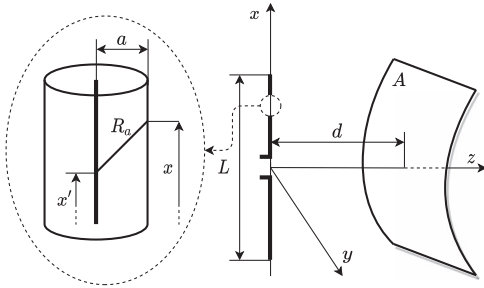


Figure 2. Half-wavelength dipole of length L and radius a placed in free space. The evaluation surface of area A on which the EM field is computed is set at a separation distance d from the antenna.

where $I(x')$ is the current distribution along the dipole, $g_a(x, x')$ is the integral equation kernel in free space

$$g_a(x, x') = \frac{\exp(-jkR_a)}{R_a}, \quad (2)$$

and R_a represents the Euclidian distance from the source point at the centre of the dipole, x' , to the observation point on the outer layer of the dipole, x , as shown in Figure 2. Other parameters in Equation 1 are angular frequency, ω , permeability of free space, μ_0 and permittivity of free space, ϵ_0 , while in Equation 2, k represents the wave number.

The spatial domain is discretised using 51 wire segment with a set to correspond to one-tenth of a single segment's length. The solution of Equation 1 is carried out by the Galerkin–Bubnov indirect boundary element method⁽³³⁾. Current distribution along the dipole at $f = 60$ GHz is shown in Figure 3(a).

Due to the finite number of wire segments, the accuracy of the solution is compromised because numerical instabilities may occur at edge segments as well as in the centre segment connected to a voltage source. These instabilities are usually manifested as numerical artefacts that lead to errors in current gradient even if the current, defined as a discrete function of

space, $I(x)$, is interpolated by a piece-wise polynomial, resulting in a continuous function of space, $\hat{I}(x)$, see Figure 3(b). To avoid the non-physical patterns in the current gradient distribution, the current is fitted with a simple feed-forward neural network, schematically shown in Figure 3(c). The neural network is consisted of three fully-connected layers with 128, 256 and 128 units, each activated using a tanh activation function. The computer implementation of the network is done through JAX⁽³⁴⁾, Python-based, extensible system for transforming numerical functions. Two most important transformations in this case are automatic differentiation of native Python functions and just-in-time compilation powered by XLA (Accelerated Linear Algebra). Training of the neural network is done using the Adam optimiser⁽³⁵⁾ with the learning rate of 0.001 over 10 000 iterations. Learning curves are shown in Figure 3(d). Trained neural network, $\text{NN}(x; \Theta^*)$, where Θ^* is the set of learned parameters, i.e., connection weights between units of the network, is then used to approximate the current along the dipole, shown in Figure 3(e).

Sharp spikes of the current gradient at critical segments on the dipole occur using finite difference approach with either discrete or continuous variant of the current as the function of space, see Figure 4(a).

Instead, by enforcing automatic differentiation on $\text{NN}(x; \Theta^*)$ with respect to x , we are able to ‘smooth out’ sharp gradient spikes, Figure 4(b), and ensure an accurate EM simulation that follows.

EM field computation

Once the current and current gradient distribution along the dipole are computed, the electric field can be evaluated from the integral equations⁽³³⁾

$$E_x = \frac{1}{j4\pi\omega\epsilon_0} \left(\int_L \frac{\partial I(x')}{\partial x'} \frac{\partial g(x, y, z, x')}{\partial x} dx' - k^2 \int_L I(x') g(x, y, z, x') dx' \right), \quad (3)$$

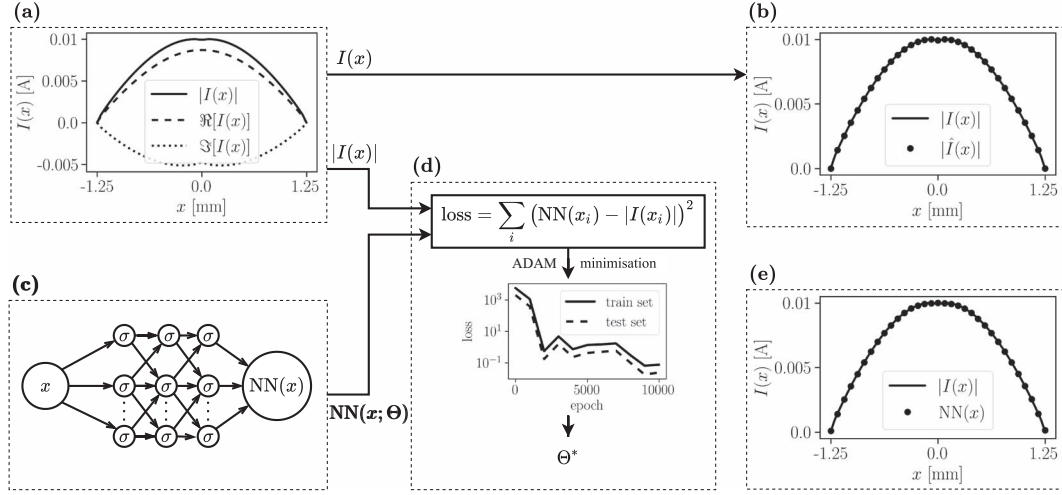


Figure 3. ML-assisted antenna modelling workflow overview: (a) current distribution along the dipole at 60 GHz, (b) cubic spline interpolation of the current as a function of space, (c) three-layer feed-forward neural network used for functional approximation of the current, (d) loss function minimisation, (e) neural network approximation of the current.

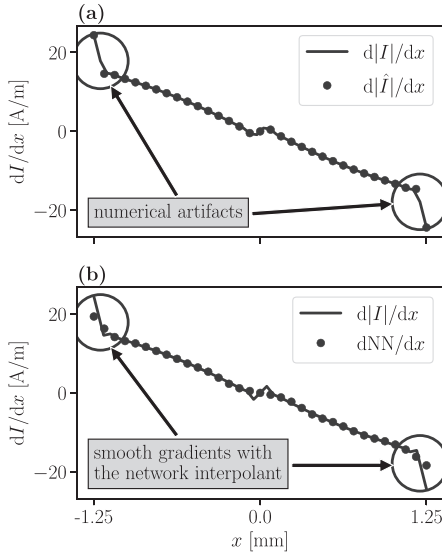


Figure 4. Distribution of the current gradient along the dipole at 60 GHz where the current is approximated with (a) cubic spline interpolation, (b) neural network.

$$E_y = \frac{1}{j4\pi\omega\epsilon_0} \int_L \frac{\partial I(x')}{\partial x'} \frac{\partial g(x, y, z, x')}{\partial y} dx', \quad (4)$$

$$E_z = \frac{1}{j4\pi\omega\epsilon_0} \int_L \frac{\partial I(x')}{\partial x'} \frac{\partial g(x, y, z, x')}{\partial z} dx', \quad (5)$$

where $g(x, y, z, x')$ is the free space Green function

$$g(x, y, z, x') = \frac{\exp(-jkR)}{R}, \quad (6)$$

and R is the distance between the dipole and the point at which the field is computed. According to the Maxwell–Faraday equation⁽³³⁾, a spatially varying, non-conservative electric field is inseparable from the magnetic field, whose components, in the case of a dipole, are given as follows:

$$H_y = \frac{1}{4\pi} \int_L I(x') \frac{\partial g(x, y, z, x')}{\partial z} dx', \quad (7)$$

$$H_z = -\frac{1}{4\pi} \int_L I(x') \frac{\partial g(x, y, z, x')}{\partial y} dx'. \quad (8)$$

EM field Equation (3) to (5), (7) and (8) are computed numerically where integration is approximated using the Gauss-Legendre quadrature⁽³⁶⁾.

Post-processing

The spatially averaged IPD is defined as the surface integral of the normal component of the time-averaged Poynting vector in free space⁽³⁷⁾

$$sPD_n = \frac{1}{2A} \iint_A \Re[E \times H^*] \cdot \mathbf{n} dA, \quad (9)$$

where E and H are peak values of the complex phasor electric and magnetic field, respectively, $*$ is the complex conjugate operator, \mathbf{n} is the unit vector field normal to the averaging surface of area A and dA is the differential area element.

The unit vector field normal to the evaluation plane of the planar model contains only y -direction components, see Figure 1(a) for reference. The expression for IPD spatially averaged on the planar model can thus be simplified to

$$sPD_n = \frac{1}{2A} \iint \Re[E_x H_z] dx dz. \quad (10)$$

A reference coordinate system should be transformed from Cartesian (x, y, z) to either spherical (r, θ, φ) or cylindrical (r, θ, z) depending on the shape of a non-planar model to seamlessly construct a parametric representation of a three-dimensional (3-D) evaluation surface in 2-D space. In case of the spherical coordinate system (ISO 80000-2:2019), r represents the radial distance (the distance to origin), θ is the polar angle and φ is the angle of rotation from the initial meridian plane (azimuthal angle). Components of the cylindrical coordinate system (ISO 80000-2:2019) are the radial distance, r , the azimuthal angle, φ and the axial coordinate, z . The construction of the parametric integration surface over which the flux in Equation 9 should be estimated is trivial after appropriate coordinate transformation. Note that even though the area of all averaging surfaces embedded in 3-D space is the same, this is not the case for a 2-D parametric integration space where areas may differ.

In⁽²⁸⁾, it has been shown that the spatially averaged IPD on a parametric spherical averaging surface, $v(\theta, \varphi)$, is given as

$$sPD_n = \frac{1}{A} \iint S(v) \cdot (v_\theta \times v_\varphi) d\theta d\varphi, \quad (11)$$

where $v_\theta \times v_\varphi$ is the cross product between partial derivatives of the parametric surface which results in the vector normal to the tangent plane at a particular point.

On the other hand, the parametric evaluation plane of the cylindrical model is given as

$$v(\varphi, z) = r \cos(\varphi) \hat{e}_x + r \sin(\varphi) \hat{e}_y + z \hat{e}_z \quad (12)$$

and the corresponding unit normal vector field is defined as

$$n = -\frac{v_\varphi \times v_z}{|v_\varphi \times v_z|}, \quad (13)$$

where $v_\varphi \times v_z$ is the cross product between partial derivatives of the parametric surface. From here, Equation 9 is re-written as

$$\begin{aligned} sPD_n &= \frac{1}{A} \iint S(v) \cdot \frac{v_\varphi \times v_z}{|v_\varphi \times v_z|} |v_\varphi \times v_z| d\varphi dz \\ &= \frac{1}{A} \iint S(v) \cdot (v_\varphi \times v_z) d\varphi dz. \end{aligned} \quad (14)$$

To numerically compute the surface integrals in Equation (10), (11) and (14), the Gauss quadrature is utilised in 2-D. The total flux across the parametric evaluation plane is computed by adding up incremental contributions on integration nodes selected as roots of the 11th degree Legendre polynomials, scaled with proper weights derived for each corresponding node⁽³⁶⁾. The quadrature degree is chosen as the optimal ratio of the computational cost and the accuracy of the final result⁽³⁸⁾.

Results and discussion

This section is dedicated to the computational results where sPD_n is evaluated in different exposure scenarios. sPD_n is computed at antenna-to-head separation distance, d , ranging from 2 to 150 mm at 6, 26, 60, and 90 GHz. The curvature of a non-planar surface is controlled by its radius, r_c , where by increasing r_c , the curvature becomes less pronounced. In this study, r_c is set within the range of 5–15 cm. The spatial averaging is performed over the 2-D integration plane that corresponds to the planar projection of a non-planar averaging surface of either 4 cm² at $f \in [6, 30]$ GHz or 1 cm² at $f > 30$ GHz to act in accordance with the ICNIRP guidelines⁽⁸⁾ and IEEE/ICES standard⁽⁹⁾.

Effect of antenna-to-tissue separation distance

In Figure 5, it is shown that with an increase in d , sPD_n decreases monotonically for all averaging surfaces regardless of r_c at each f considered in the analysis.

The largest captured sPD_n is 27.86 W m⁻², computed on a spherical model with $r_c = 5$ cm at $d = 2$ mm and $f = 90$ GHz. The same exposure set-up results in $sPD_n = 26.80$ W m⁻² on the cylindrical surface which is only slightly greater compared with the planar surface ($sPD_n = 26.40$ W m⁻²). The difference in sPD_n between models is marginal at $d \geq 50$ mm with $sPD_n < 0.3$ W m⁻² in all cases.

In Figure 6, the relative percentage difference (RPD) between sPD_n on the spherical and planar, and between sPD_n on the cylindrical and planar averaging surface is shown.

Note that the reference sPD_n value is computed on a corresponding planar model for all cases. By increasing d , RPD between sPD_n on the spherical and planar surface decays monotonically towards at most 0.14% and 1.35% corresponding to $r_c = 15$ cm and $r_c = 5$ cm, respectively. Interestingly, at 6 GHz, an increase in d leads to slight decay in RPD between sPD_n on the cylindrical and planar surface up to $d = 10$ mm, followed by a sudden increase in RPD at $d = 10$ mm and expected monotonic decay afterwards. For the rest

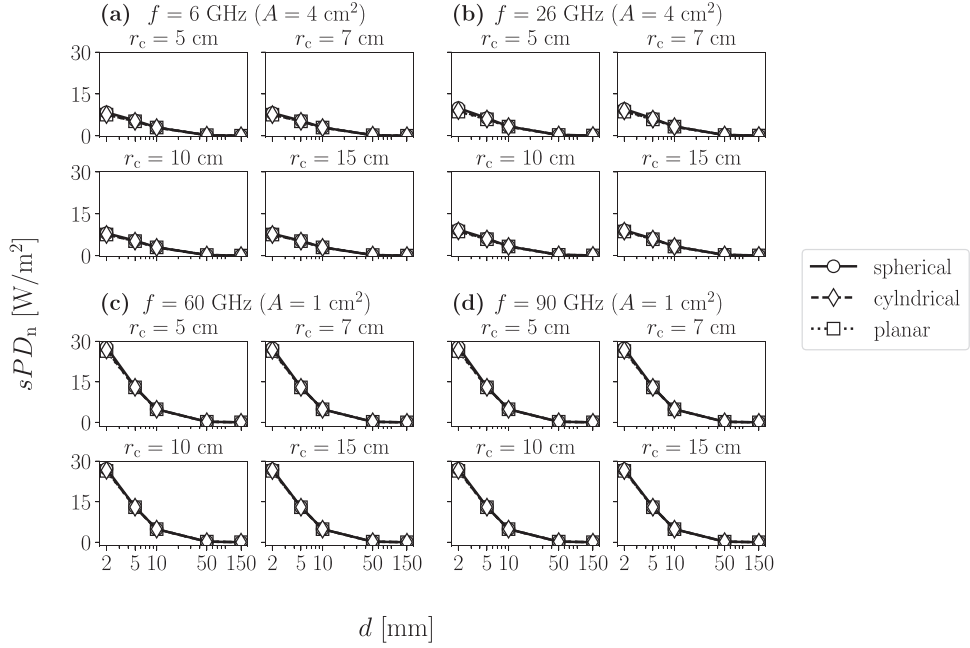


Figure 5. Spatially averaged IPD as a function of the separation distance over the spherical (round markers), cylindrical (diamond markers) and planar (square markers) surface for various curvature radii at (a) 6 GHz, (b) 26 GHz, (c) 60 GHz and (d) 90 GHz.

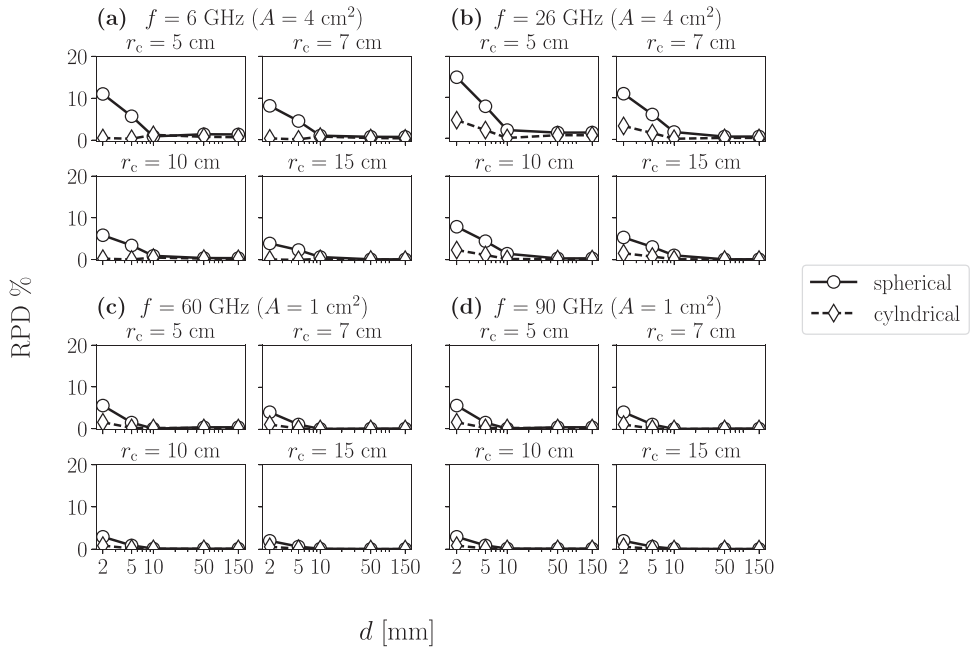


Figure 6. RPD in the spatially averaged IPD as a function of the separation distance between the spherical and planar (round markers), and between the cylindrical and planar (diamond markers) averaging surface for various curvature radii at (a) 6 GHz, (b) 26 GHz, (c) 60 GHz and (d) 90 GHz.

of the frequencies, RPD in sPD_n between the cylindrical and planar surface decays monotonically with increasing d towards at most 0.07% and 0.69% corresponding to $r_c = 15$ cm and $r_c = 5$ cm, respectively. In all cases, RPD becomes negligible (within 1.35%) at $d \geq 50$ mm regardless of f and r_c . On the other hand, RPD is pronounced in the near field, especially at $d = 2$ mm, where the maximum RPD of 14.88% is captured at 26 GHz for the case of the spherical surface with $r_c = 5$ cm.

Effect of curvature radius

With an increase in r_c from 5 to 15 cm, sPD_n decays for a corresponding surface at fixed f and d . The largest decay of 0.94 W m^{-2} is captured on the spherical surface at $d = 2$ mm and $f = 60$ and 90 GHz. This decay in sPD_n is marginal on the cylindrical surface because the curvature in that case is generally less emphasised and therefore has less impact during integration. The findings suggest relatively strong positive correlation between the curvature of averaging surfaces and the value of sPD_n — smaller r_c , greater overall curvature, greater sPD_n . The effect of curvature can most likely be explained by considering the spatial distribution of the unit vector field normal to averaging surfaces. Namely, averaging over a planar surface is performed by integrating contributions of the power density considering only a single component of the unit vector field normal to the surface. On the other hand, averaging over both spherical and cylindrical surfaces must be performed by including all components of the unit normal vector field. The largest RPDs are captured between the spherical and planar surface at 26 GHz, see Figure 7(a).

Here, RPD as a function of d and r_c is maximal at $d = 2$ mm and $r_c = 5$ cm. In, Figure 7(b), identical behaviour is present for the case of the cylindrical surface only to a lesser extent since only one spatial coordinate (azimuthal angle) affects the non-planarity of the surface. However, at $d = 10$ mm for $r_c = 5$ and 7 cm, RPD deviates from the expected values with a sudden drop to a negligible difference in comparison with the planar surface. In Figure 8, it is shown that an increase in r_c leads to an exponential decay in RPD in all cases except on the cylindrical surface with $r_c = 5$ and 7 cm at $d = 10$ mm.

Effect of frequency

An increase in f from 6 to 26 GHz leads to an increase in sPD_n . This increase undergoes an exponential decay as d increases for a fixed r_c . Between 30 and 60 GHz, sPD_n is increased only slightly (about 0.1 W m^{-2}) for identical surfaces at corresponding d . In⁽²⁸⁾, it is hypothesised that this phenomena occurs because the beam is focused on a limited area of the control surface.

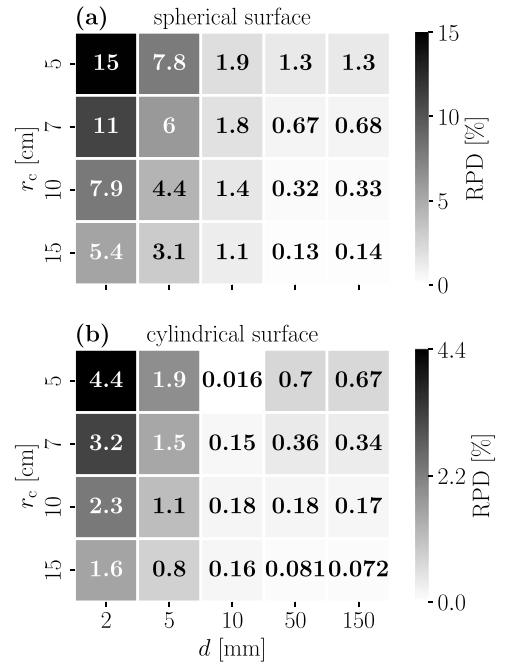


Figure 7. Heat-map of RPDs in the spatially averaged IPD at 26 GHz as a function of the separation distance and curvature radius between (a) the spherical and planar surface, (b) the cylindrical and planar surface.

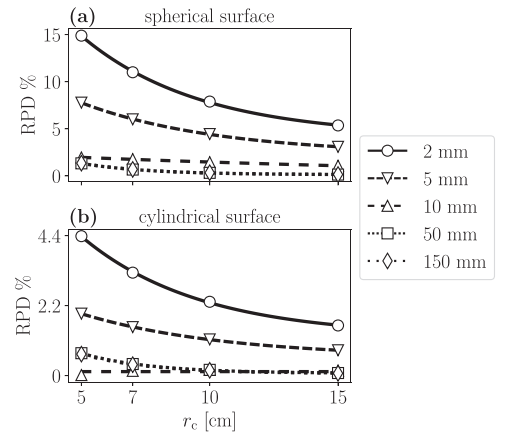


Figure 8. RPD at 26 GHz in the spatially averaged IPD as an exponential function of the curvature radius at separation distances ranging from 2 to 150 mm between the antenna and (a) spherical, (b) cylindrical surface.

Although the power density is significantly higher in the aforementioned area, the magnitude of this effect is relaxed during spatial integration by taking into account the control surface in the entirety.

Conclusion

This paper introduced the idea of ML and its corresponding techniques to extenuate numerical artefacts ubiquitous in conventional antenna modelling and associated EM simulations. As a proof of concept, non-planar body parts were irradiated by a half-wavelength dipole antenna at 6–90 GHz. To limit the exposure, the spatially averaged IPD was used as a free space approximation of APD above 6 GHz, a surrogate for maximum skin temperature elevation. The analysis of IPD spatially averaged on control surfaces of two different canonical non-planar tissue models, i.e., a sphere and a cylinder, has been provided. The findings suggest that the curvature of the model is positively correlated with the value of the spatially averaged IPD. Overall this paper offers two essential contributions to exposure assessment protocols and the computational bioelectromagnetics in general: (i) the introduction of the differentiable programming which facilitates modelling and allows more accurate simulations, and (ii) the spatial averaging of power densities above 6 GHz on non-planar surfaces which lies ahead as a challenge currently discussed within a working group 7 of IEEE TC 95 SC 6 on EM dosimetry modelling.

Funding

This research was supported by the European Regional Development Fund [KK.01.1.1.01.0009 (DATACROSS)].

Data availability

All the code and data used for the analysis are available upon request to the corresponding author.

References

1. Wu, T., Rappaport, T. and Collins, C. Safe for generations to come: considerations of safety for millimeter waves in wireless communications. *IEEE Microw. Mag.* **16**(2), 65–84 (2015).
2. 3rd Generation Partnership Project (3GPP). NR; *User Equipment (UE) radio transmission and reception; Part 1: Range 1 Standalone* Technical Specification (TS) 38.101-1, Release 17.7.0. (2022).
3. 3rd Generation Partnership Project (3GPP). NR; *User Equipment (UE) radio transmission and reception; Part 2: Range 2 Standalone* Technical Specification (TS) 38.101-2, Release 17.7.0. (2022).
4. Rappaport, T., Sun, S., Mayzus, R., Zhao, H., Azar, Y., Wang, K., Wong, G., Shulz, J., Samimi, M. and Gutierrez, F. Millimeter wave mobile communications for 5G cellular: it will work! *IEEE Access.* **1**, 335–349 (2013).
5. Hirata, A. et al. Assessment of human exposure to electromagnetic fields: review and future directions. *IEEE Trans. Electromagn. Compat.* **63**(5), 1619–1630 (2021).
6. Alekseev, S., Radzievsky, A., Logani, M. and Ziskin, M. Millimeter wave dosimetry of human skin. *Bioelectromagnetics* **29**, 65–70 (2008).
7. Zhadobov, M., Chahat, N., Sauleau, R., Le Quement, C. and Le Drian, Y. Millimeter-wave interactions with the human body: state of knowledge and recent advances. *Int. J. Microw. Wirel. Technol.* **3**, 237–247 (2011).
8. International Commission on Non-Ionizing Radiation Protection (ICNIRP). Guidelines for limiting exposure to electromagnetic fields (100 kHz to 300 GHz). *Health Phys.* **118**, 483–524 (2020).
9. *IEEE standard for safety levels with respect to human exposure to electric, magnetic, and electromagnetic fields, 0 Hz to 300 GHz* IEEE Std C95.1-2019 (Revision of IEEE Std C95.1-2005/Incorporates IEEE Std C95.1-2019/Cor 1-2019). IEEE, pp. 1–312 (2019).
10. Hirata, A. and Shiozawa, T. Correlation of maximum temperature increase and peak SAR in the human head due to handset antennas. *IEEE Trans. Microwave Theory & Tech.* **51**, 1834–1841 (2003).
11. Razmadze, A., Shoshiashvili, L., Kakulia, D., Zaridze, R., Bit-Babik, G. and Faraone, A. Influence of specific absorption rate averaging schemes on correlation between mass-averaged specific absorption rate and temperature rise. *Electromagnetics* **29**, 77–90 (2009).
12. McIntosh, R. and Anderson, V. SAR versus S_{inc} : what is the appropriate RF exposure metric in the range 1–10 GHz? Part II: using complex human body models. *Bioelectromagnetics* **31**, 467–478 (2010).
13. Hashimoto, Y., Hirata, A., Morimoto, R., Aonuma, S., Laakso, I., Jokela, K. and Foster, K. On the averaging area for incident power density for human exposure limits at frequencies over 6 GHz. *Phys. Med. Biol.* **62**, 3124 (2017).
14. Foster, K., Ziskin, M. and Balzano, Q. Thermal response of human skin to microwave energy: a critical review. *Health Phys.* **111**, 528–541 (2016).
15. Hirata, A., Funahashi, D. and Kodera, S. Setting exposure guidelines and product safety standards for radio-frequency exposure at frequencies above 6 GHz: brief review. *Ann. Telecommun.* **74**, 17–24 (2019).
16. Gandhi, O. and Riaz, A. Absorption of millimeter waves by human beings and its biological implications. *IEEE Trans. Microw. Theory Techn.* **34**(2), 228–235 (1986).
17. Walters, T., Blick, D., Johnson, L., Adair, E. and Foster, K. Heating and pain sensation produced in human skin by millimetre waves: comparison to a simple thermal model. *Health Phys.* **78**, 259–267 (2000).
18. Kojima, M., Susuki, Y., Sasaki, K., Taki, M., Wake, K., Watanabe, S., Mizuno, M., Tasaki, T. and Sasaki, H. Ocular effects of exposure to 40, 75 and 95 GHz millimeter waves. *J. Infrared, Millimeter and Terahertz Waves.* **39**(9), 912–925 (2018).
19. He, W., Xu, B., Gustafsson, M., Ying, Z. and He, S. RF compliance study of temperature elevation in human head model around 28 GHz for 5G user equipment application: simulation analysis. *IEEE Access.* **6**, 830–838 (2018).

20. Colombi, D., Thors, B., Törnevik, C. and Balzano, Q. RF energy absorption by biological tissues in close proximity to mmW 5G wireless equipment. *IEEE Access*. **6**, 4974–49821 (2018).
21. Poljak, D. and Cvetković, M. *On the incident power density calculation in GHz frequency range: a case of Hertz dipole*. In *Proceedings of the 4th International Conference on Smart and Sustainable Technologies (SpliTech)*. Split, Croatia: IEEE, pp. 1–4, (2019).
22. Li, K., Sasaki, K., Watanabe, S. and Shirai, H. Relationship between power density and surface temperature elevation for human skin exposure to electromagnetic waves with oblique incidence angle from 6 GHz to 1 THz. *Phys. Med. Biol.* **64**(5), 065016 (2019).
23. Samaras, T. and Kuster, N. Theoretical evaluation of the power transmitted to the body as a function of angle of incidence and polarization at frequencies > 6 GHz and its relevance for standardization. *Bioelectromagnetics* **40**(2), 136–139 (2019).
24. Nakae, T., Funahashi, D., Higashiyama, J., Onishi, T. and Hirata, A. Skin temperature elevation for incident power densities from dipole arrays at 28 GHz. *IEEE Access*. **8**, 26863–26871 (2020).
25. Li, K., Diao, Y., Sasaki, K., Prokop, A., Poljak, D., Doric, V., Xi, J., Kodera, S., Hirata, A. and El Hajj, W. Intercomparison of calculated incident power density and temperature rise for exposure from different antennas at 10–90 GHz. *IEEE Access*. **9**, 151654–151666 (2021).
26. Li, K., Sasaki, K., Wake, K., Onishi, T. and Watanabe, S. Quantitative comparison of power densities related to electromagnetic near-field exposures with safety guidelines from 6 to 100 GHz. *IEEE Access*. **9**, 115801–115812 (2021).
27. Sacco, G., Haider, Z. and Zhadobov, M. Exposure levels induced in curved body parts at mmWaves. *IEEE J. Electromagn. RF microw. Med. Biol.* **6**(3), 413–419 (2022).
28. Lojic Kapetanovic, A. and Poljak, D. Assessment of incident power density on spherical head model up to 100 GHz. *IEEE Trans. Electromagn. Compat.* **64**(5), 1296–1303 (2022).
29. Innes, M., Edelman, A., Fischer, K., Rackauckas, C., Saba, E., Shah, V. and Tebbutt, W. A differentiable programming system to bridge machine learning and scientific computing arXiv preprint. (2019).
30. Baydin, A., Pearlmutter, B., Radul, A. and Siskind, J. Automatic differentiation in machine learning: a survey. *J. Mach. Learn. Res.* **18**(1), 5595–5637 (2018).
31. Lojic Kapetanovic, A. and Poljak, D. *Application of automatic differentiation in electromagnetic dosimetry - assessment of the absorbed power density in the mmWave frequency spectrum*. In *Proceedings of the 6th International Conference on Smart and Sustainable Technologies (SpliTech)*, Bol and Split, Croatia, pp. 1–6 (2021).
32. Hirata, A., Kodera, S., Sasaki, K., Gomez-Tames, J., Laakso, I., Wood, A., Watanabe, S. and Foster, K. Human exposure to radiofrequency energy above 6 GHz: review of computational dosimetry studies. *Phys. Med. Biol.* **66**, 08TR01 (2021).
33. Poljak, D. *Advanced modeling in computational electromagnetic compatibility, ch. 8.1*. (Hoboken, New Jersey: John Wiley & Sons, Inc.) (2006) ISBN 978-0470036655.
34. Bradbury, J. et al. *JAX: composable transformations of Python+NumPy programs*. (2018).
35. Kingma, D. and Ba, J. *Adam: a method for stochastic optimization*. In *Proceedings of the 3rd International Conference for Learning Representations (ICLR)*, San Diego, USA, pp. 1–15 (2015).
36. Abramowitz, M. and Stegun, I. *Handbook of mathematical functions with formulas, graphs, and mathematical tables, ch. 25.4.29*. (New York, USA: Dover Publication, Inc.) (1972) ISBN 978-1614276173.
37. *IEEE guide for the definition of incident power density to correlate surface temperature elevation* IEEE Std 2889-2021. pp. 1–152 (2021).
38. Lojic Kapetanovic, A., Sacco, G., Poljak, D. and Zhadobov, M. *Assessment of area-average absorbed power density on realistic tissue models at mmWaves*. In *Proceedings of the 2022 IEEE MTT-S International Microwave Biomedical Conference (IMBioC)*, Suzhou, Chime, pp. 153–155 (2022).